

Neutrons from radiative pion capture in carbon, oxygen, and calcium*

W-C. Lam,† K. Gotow, B. MacDonald,‡ and W. P. Trower

Physics Department, Virginia Polytechnic Institute and State University, Blacksburg, Virginia 24061

(Received 28 January 1974)

The energy spectra of neutrons between 2 and 28 MeV emitted following radiative pion capture in carbon, oxygen, and calcium fall off exponentially. An enhancement, however, is observed for neutron energies below 5 MeV in carbon and oxygen. Neutron yield peaks at n - γ angles of 180° , indicating a quasifree absorption mechanism in this process.

NUCLEAR REACTIONS $^{12}\text{C}(\pi^-, n\gamma)$, $^{16}\text{O}(\pi^-, n\gamma)$, $^{40}\text{Ca}(\pi^-, n\gamma)$, $E = 0$ MeV; measured reaction rate, neutron energy spectrum, and n - γ angular correlations; deduced giant resonance states and direct emission contributions.

I. INTRODUCTION

Nuclear absorption of negative pions from atomic orbits results, 1 to 3% of the time, in a photon being emitted with an energy nearly equal to that of the pion rest mass. This process, radiative pion absorption, was first observed by Petrukhin and Prokoshkin.¹ Subsequently, the photon energy spectrum and branching ratios for various elements were measured.¹⁻³ The effective interaction for radiative pion capture is dominated by an axial vector term^{4,5}; thus, the resulting excitations are similar to those in electromagnetic scattering and muon capture.

Three processes are responsible for neutrons emitted following radiative capture: If capture takes place on a single bound proton,

$$\pi^- + p \rightarrow n + \gamma, \quad (1)$$

then a neutron with a kinetic energy of about 9 MeV will be produced in a direction opposite to that of the photon. Even with the proton's Fermi motion the neutron will display the characteristic kinematics of (1).^{6,7} We call these neutrons "direct emission neutrons."

Neutrons can be produced by the decay of nuclear excited states

$$\pi^- + (A, Z) \rightarrow (A, Z-1)^* + \gamma \rightarrow (A-1, Z-1)^* + \gamma + n \quad (2)$$

which are primarily giant resonance analog states.^{8,9} This mechanism involves intermediate states which are reasonably well defined and thus will be coherent with the direct emission process. These resonance emission neutrons have kinetic energies¹⁰ and neutron-photon (n - γ) angular correlations characteristic of the decaying state.

The third process occurs when a large energy is

transferred to the nucleus by either the pion absorption or the rescattering of the outgoing neutron. Deexcitation of the nucleus can proceed by the isotropic evaporation of neutrons with very low kinetic energies.

Here we report the result of an experiment in which we obtained two dimensional distributions of the energy and n - γ angle for neutrons following radiative pion capture by carbon, oxygen, and calcium.

II. EXPERIMENTAL DETAILS

A. Experimental setup and electronic logic

The experimental setup, which used a 100 MeV negative pion beam from the Space Radiation Effects Laboratory 600 MeV synchrocyclotron, is shown in Fig. 1. The beam telescope contained plastic scintillation counters 1, 2, 3, and 4 and a water Cerenkov counter (C). High energy photons from radiative pion capture were detected in seven lead-glass total absorption Cerenkov counters, placed at various n - γ angles between 26° and 165° . The target faced the neutron counter minimizing flight path differences of neutrons originating from different sites. The counters which bracketed the target were kept out of view of the neutron counter because the n - γ coincidence rate from hydrogen in the scintillators was 100 times larger than from our target nuclei.

Pions traversed the beam telescope, were slowed down in an absorber, and stopped in the target. The radiative pion capture event signal was a coincidence between a stopping pion signal ($1\bar{C}23\bar{4}$) and a signal from one of the seven lead-glass counters (γ_i). The electronic logic is shown in Fig. 2(a). The neutron energy was found using a time-to-amplitude converter (TAC) gated with a

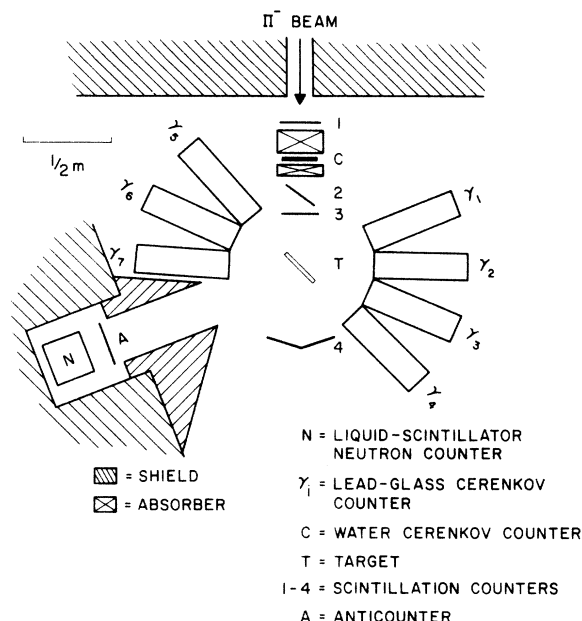


FIG. 1. Schematic of the experimental apparatus. A radiative pion capture event trigger was $1C234\gamma_i$.

linear gate (LG) by a signal from the neutron pulse shape discrimination circuit which set the neutron counter threshold and rejected γ -ray-induced signals. The time-of-flight information and the tagging signals and pulse heights of the γ counters were fed into an IBM 360/44 computer through an IBM Scientific Nuclear Interface (SICU). The tagging signal also routed the TAC pulse height into different sections of a pulse height analyzer (PHA) memory which was used as a backup and monitoring device.

B. γ counters

A γ counter, a piece of lead glass $43.2 \times 15.2 \times 20.3$ cm³, converted photons to charged particles. The resulting Cerenkov radiation was collected by two arrays, A and B, of seven RCA 6655 photomultipliers from which both the anode (A) and dynode (D) outputs were used. A schematic is seen in Fig. 2(b).

The γ counters were calibrated using an electron beam. Figure 3 shows two extreme examples of γ counter efficiency. The fractional resolution

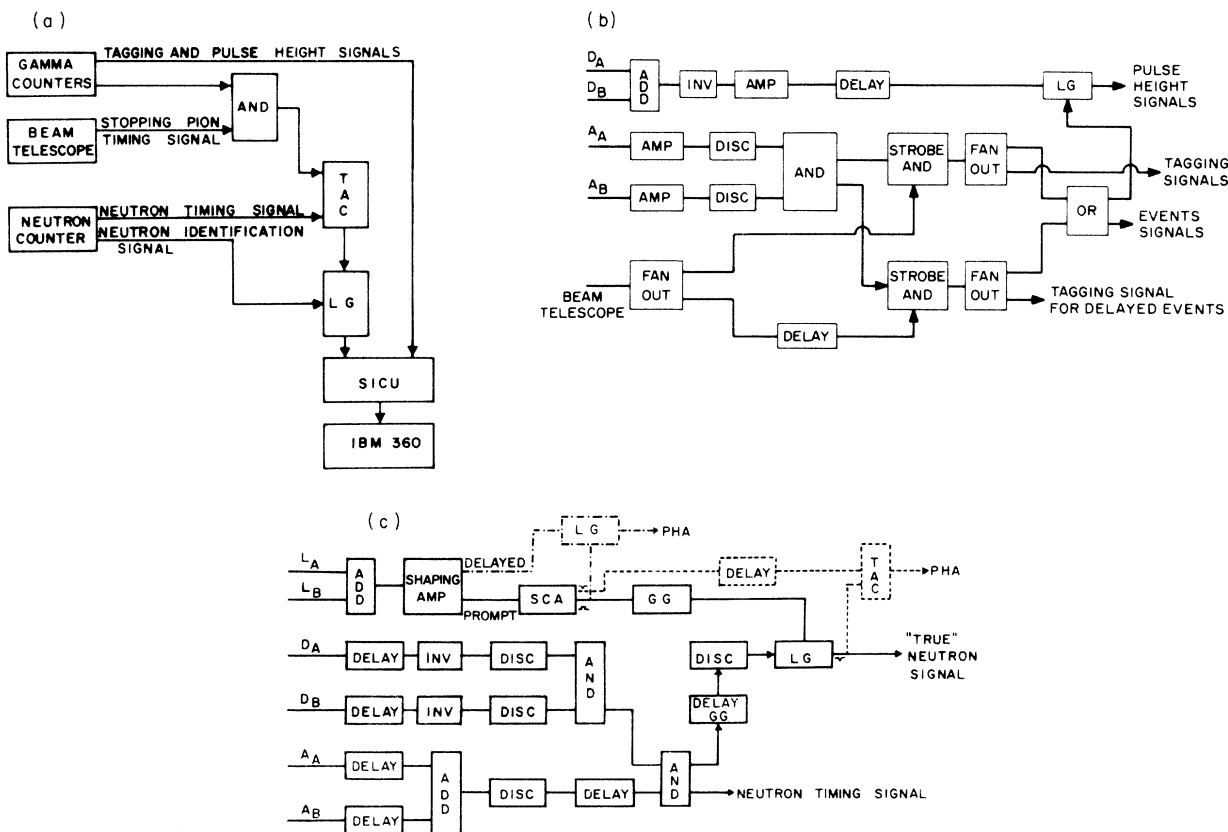


FIG. 2. Schematic of electronic logic. (a) Data collection. (b) Detail of the γ counter electronics. (c) Detail of the neutron counter electronics. The circuit (----) monitors the n - γ discrimination while (- - - -) checks the neutron counter threshold.

thus measured was an optimistic estimate, as the photons in the experiment diverged in the counters.

C. Neutron counter

The $30.5 \times 30.5 \times 17.8$ cm³ active volume of the neutron counter was filled with NE213 liquid scintillator and was viewed in coincidence by two 58 AVP photomultipliers, (A) and (B). A n - γ pulse shape discriminator using a linear output (L),¹¹ a high-low threshold timing using dynode (D) and anode (A) signals, and a coincidence between A and B to reduce accidentals due to the tube noise were included in the neutron counter electronics seen in Fig. 2(c). The neutron counter threshold was set at 100 keV in electron energy using a ²²Na source: the Compton edge at 0.34 MeV and the 1.27 MeV photopeak.

The energy dependent neutron counter efficiency was calculated by a computer code designed for counters with cylindrical geometry.¹² We approximated our counter by the one shown in Fig. 4(a). For a large counter the dependence of efficiency on the lateral dimension is small because the mean free path of the recoil charged particle in the scintillator is very much less than the average escape distance. The efficiency for 20 MeV neutrons in cylindrical counters with radii of 15 and 17 cm differed by 2%. Neutron efficiencies at 20 energies between 1 and 30 MeV were calculated with 5000 events per point. The curve fitted to these points is displayed in Fig. 4(b).

D. Targets

All targets were kept scrupulously free of hydrogenous materials. The carbon target, a piece of graphite 22.9 cm square and 4.76 cm thick, was baked at 200°C for a day to dehydrate it before it

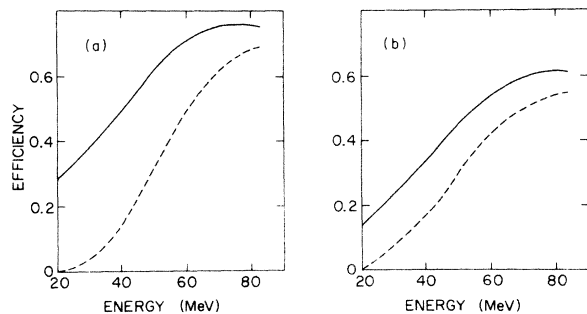


FIG. 3. γ counter efficiency as a function of energy for the two extreme counters. The fractional resolution (FWHM) for 80 MeV electrons is (a) 59% and (b) 123%. The energy scale is uncertain by ± 10 MeV. The solid (broken) curve is the efficiency determined by the anode threshold (for a 55 MeV threshold set by the dynode pulse height).

was wrapped in 0.05 mm aluminum foil. The calcium target, desiccated commercial grains, was sealed in an air tight aluminum can with ~ 0.25 mm thick walls. The liquid oxygen target, 5.08 cm thick, was surrounded by a cooling jacket through which boil-off nitrogen circulated. The oxygen container was an aluminum flask, the front and back face of which were 0.8 mm while the sides were 1.6 mm thick. About 10% of the pions were captured outside the oxygen.

E. Backgrounds

The neutron counter was enclosed in a 10.2 cm thick lead shield surrounded by a paraffin block-house which reduced the singles rate to 500/s.

With counters 3 and 4 closely bracketing a 5.08 cm thick CH₂ target, 80,000 stopping pions per second resulted. With these counters moved out of view of the neutron counter, the stopping pion rate increased $\sim 30\%$. These spurious stopping signals, however, were rarely in coincidence with a γ counter signal.

III. DATA REDUCTION

A. Data

Four types of data were collected:

- (1) Neutron and photon energy distributions from

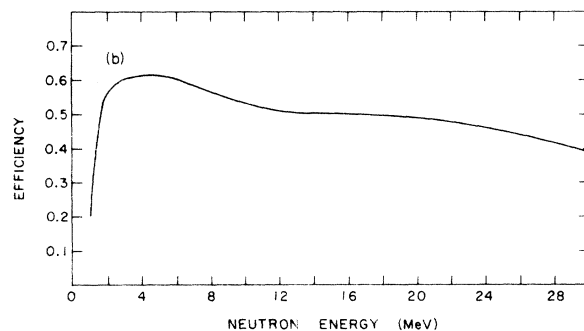
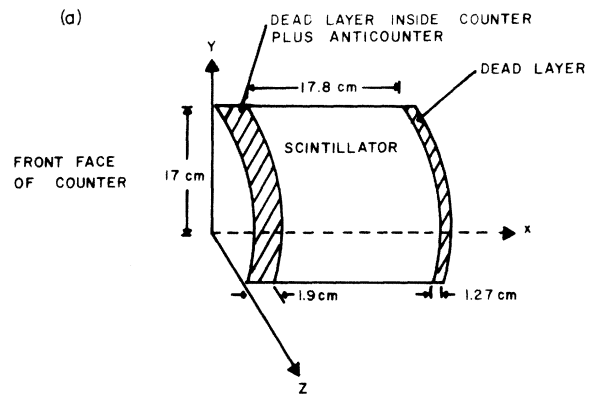


FIG. 4. (a) Cylindrical approximations used in the efficiency calculation of the neutron counter. (b) Neutron counter efficiency as a function of neutron energy.

radiative pion capture in elemental targets. For each γ counter three spectra were taken. The first had neutron flight time versus pulse heights of associated photons, while the second and third had photon pulse heights in coincidence with prompt and delayed stopping pion signals, respectively.

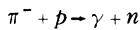
(2) Same data as above with a CH_2 target without n - γ discrimination. A γ counter was placed at 180° to the neutron counter and the spectra were used to detect radiative pion capture on hydrogen in order to obtain the energy-time conversion factor and the resolution of the neutron flight time.

(3) Neutron time-of-flight spectrum, with n - γ discrimination, following pion absorption. These data were used to subtract the accidental contribution from the radiative capture neutron energy spectrum.

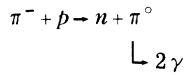
(4) Neutron time-of-flight spectrum without n - γ discrimination due to pion absorption in the target. These data were used to study the effects of the energy dependence of n - γ discrimination on the neutron detection efficiency and to monitor the stability of the time-of-flight system.

B. Calibration of time of flight

Stopping pion capture on hydrogen results in two reactions which completely calibrated the neutron time of flight to an energy scale. The reaction



produced a monoenergetic neutron (8.9 MeV and $\beta_1 = 0.137$) while



gave two photons. Signals from the neutron counter and a diametrically placed γ counter in coincidence signified that a pion had been captured on hydrogen. The TAC analog outputs H_1 , which corresponded to neutrons, and H_2 , which corresponded to photons, were given by

$$H_1 = A(C + D\beta_1^{-1}) \quad \text{and} \quad H_2 = A(C + Dc^{-1}),$$

where c is the velocity of light, D is the length of the flight path, A is a conversion constant, C is the arbitrary constant time delay between the signals from the beam telescope and neutron counter, and the neutron velocity β corresponding to some TAC pulse height H is given by

$$\beta = \frac{R - 1}{Rc^{-1} - \beta_1^{-1}},$$

where

$$R = \frac{H - H_1}{H - H_2},$$

which is independent of A and D .

Figure 5, which shows the time-of-flight spectrum recorded using a CH_2 target with the γ rejection gate removed, has prominent 8.9 MeV neutron and photon peaks whose separation yields a D of 1.62 m, which compares favorably with a measured value of 1.64 m. The width of the peaks gives the time resolution for 8.9 MeV neutrons to be 4.75 ns full width at half-maximum (FWHM) which corresponds to $\delta E \approx 1$ MeV.

C. Accidental coincidences

The observed coincidence rate between stopping pions (π_s) and neutron counter [$n(t)$] pulses can be written as

$$[\pi_s n(t)] = [\pi_s n(t)]^T + g[\pi_s][n(t)],$$

where each counting rate is indicated by a bracket, g represents the effective resolving time of the coincidence circuit, and a superscript T indicates a true rate. The neutron time-of-flight spectrum beyond the photon peak, the negative time region, was caused by the accidental rate which is the second term above.

The observed coincidence rate of stopping pion, γ counter, and neutron counter pulses is

$$\begin{aligned} [\pi_s \gamma n(t)] &= [\pi_s \gamma n(t)]^T \\ &+ g\{[\pi_s \gamma]^T [n(t)] + [\pi_s n(t)]^T [\gamma] \\ &+ [\gamma n(t)][\pi_s]\} + O(g^2) + \dots \end{aligned}$$

Now we can write

$$\begin{aligned} g[\pi_s n(t)]^T [\gamma] &= g \frac{[\pi_s n(t)]^T}{[\pi_s]} [\pi_s][\gamma] \\ &= \frac{[\pi_s n(t)]^T}{[\pi_s]} \{g[\pi_s][\gamma]\}, \end{aligned}$$

where $g[\pi_s][\gamma]$ is the observed delayed coincidence rate between stopping pion and γ counter signals, $[\pi_s \gamma]_d$.

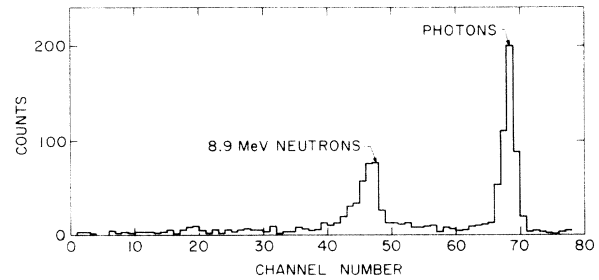


FIG. 5. Time-of-flight spectrum from a CH_2 target for neutron signals in coincidence with photon signals from the γ detector placed diametrically opposite to the neutron counter.

TABLE I. Percentage of background counts in the neutron time-of-flight spectra. The number in parenthesis is the accidentals in the photon counts.

Element	$\theta_{n\gamma}$ (deg)						
	165	155	135	112	68	48	26
Carbon	16(11)	24(16)	36(28)	50(23)	49(22)	40(22)	...
Oxygen	30(19)	37(25)	43(25)	55(29)	61(31)	50(30)	...
Calcium	33(7)	34(9)	41(9)	73(24)	51(11)	56(13)	49(10)

The accidental rate between neutron and γ counter signals not associated with a stopping pion is

$$[\gamma n(t)] = g[\gamma][n(t)].$$

Combining, we get

$$\begin{aligned} g\{[\pi_s \gamma]^T [n(t)] + [\gamma n(t)] [\pi_s]\} \\ = g[n(t)]\{[\pi_s \gamma]^T + g[\gamma][\pi_s]\} \\ = g[n(t)][\pi_s \gamma]. \end{aligned}$$

The observed coincident rate is now

$$\begin{aligned} [\pi_s \gamma n(t)] = [\pi_s \gamma n(t)]^T + \frac{[\pi_s n(t)]}{[\pi_s]} [\pi_s \gamma]_d \\ + g[\pi_s \gamma][n(t)] + O(g^2) + \dots \end{aligned}$$

The first correction term has the same time dis-

tribution as $[\pi_s n(t)]$ and is proportional to $[\pi_s \gamma]_d$, while the second is derived from the negative time spectrum.

Corrections for accidental coincidences, which depended on the target element and thresholds and characteristics of the individual photon detector, are summarized in Table I for photon counters.

D. Angular resolution

The angular resolution function for each neutron counter-target- γ counter combination was computed numerically by averaging over all points on the target and counter faces. Besides geometrical effects, the angular resolution was affected by outgoing particles interacting with the material of the target. Scattering of photons and neutrons smeared out the angular resolution function but by no more

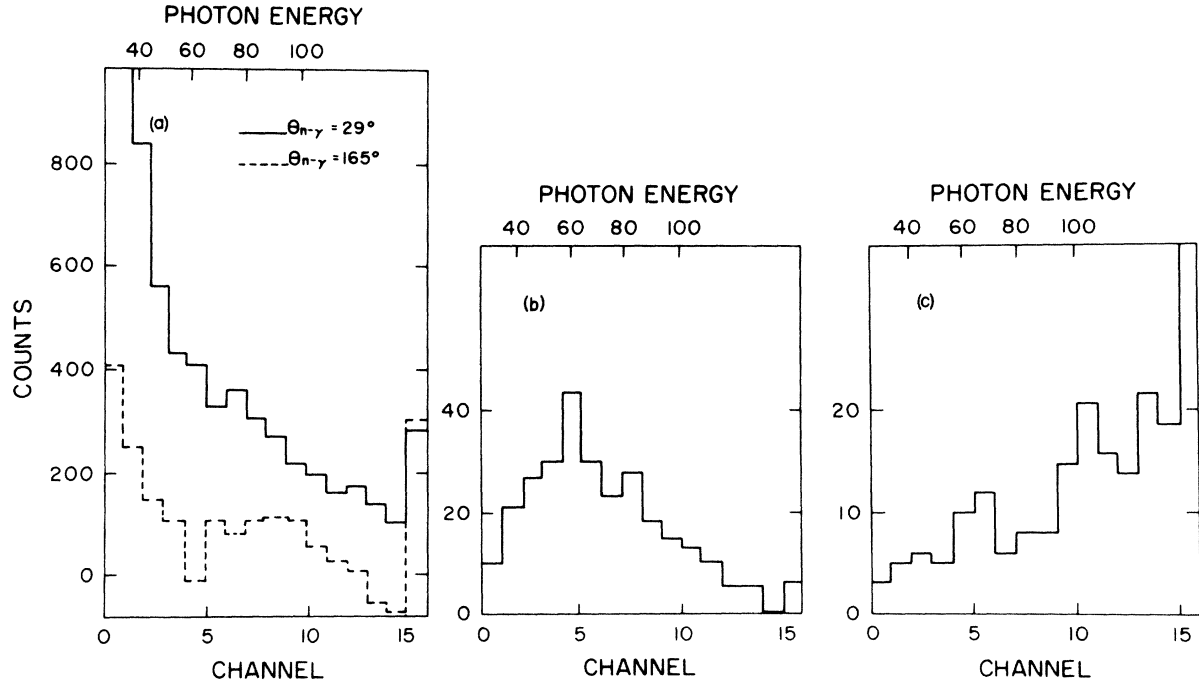


FIG. 6. (a) Typical photon energy spectra from radiative capture for two extreme γ counters using a carbon target. (b) 65 MeV photon spectrum from π^0 decay. (c) 129 MeV photon spectrum from the reaction $\pi^- p \rightarrow \gamma n$. The highest channel is the overflow counter.

TABLE IV. Neutron energy and angle distributions from Ca target: E_n indicates the lower end of the energy bin.

Neutron energy bins E_n (MeV)	Neutron yields $(N \pm \Delta N) \times 10^{-m}$ per MeV per sr per photon at various neutron-photon angles $\theta_{n\gamma}$.																	
	$\theta_{n\gamma} = 155^\circ$			$\theta_{n\gamma} = 135^\circ$			$\theta_{n\gamma} = 112^\circ$			$\theta_{n\gamma} = 68^\circ$			$\theta_{n\gamma} = 48^\circ$			$\theta_{n\gamma} = 26^\circ$		
	N	ΔN	m	N	ΔN	m	N	ΔN	m	N	ΔN	m	N	ΔN	m	N	ΔN	m
1.33	2.64	0.40	2	3.00	0.47	2	2.39	5.8	3	1.87	0.38	2	1.65	0.37	2	2.26	0.37	2
1.68	1.90	0.22	2	1.92	0.25	2	1.55	0.35	2	1.37	0.20	2	1.08	0.19	2	1.35	0.19	2
2.19	1.52	0.22	2	1.55	0.24	2	0.64	0.31	2	1.14	0.20	2	0.88	0.18	2	0.78	0.17	2
2.54	1.48	0.19	2	1.37	0.20	2	0.95	0.27	2	0.85	0.15	2	0.86	0.15	2	0.78	0.14	2
2.98	1.05	0.14	2	1.15	0.16	2	0.60	0.20	2	0.59	0.11	2	0.73	0.12	2	0.84	0.13	2
3.55	9.9	1.2	3	1.06	0.13	2	0.54	0.16	2	0.71	0.10	2	4.77	0.91	3	0.72	0.10	2
4.30	7.74	0.92	3	7.21	0.97	3	0.63	0.14	2	3.88	0.70	3	4.47	0.74	3	5.07	0.74	3
5.32	5.09	0.65	3	4.10	0.65	3	0.45	0.10	2	3.70	0.57	3	2.77	0.52	3	3.01	0.51	3
6.76	4.08	0.49	3	4.00	0.53	3	2.35	0.67	3	2.02	0.38	3	1.57	0.35	3	2.46	0.39	3
8.87	2.61	0.33	3	2.49	0.35	3	1.08	0.43	3	1.08	0.24	3	1.00	0.24	3	1.17	0.24	3
12.2	2.75	0.28	3	2.02	0.26	3	1.06	0.31	3	0.75	0.16	3	0.50	0.15	3	0.59	0.15	3
17.7	1.42	0.16	3	1.19	0.16	3	0.42	0.18	3	0.31	0.09	3	2.94	0.92	4	2.77	0.86	4

trum, we made an arbitrary choice of photon energy threshold at 55 MeV which excluded events with large backgrounds. We found that the neutron energy spectrum per photon was not sensitive to the choice of photon energy threshold. There was, however, evidence that high energy photons associate with low energy neutrons and vice versa, especially for $n\text{-}\gamma$ angles near 180° . Because of the poor energy resolution of the γ counters, we were unable to study this relationship.

2. Neutron energy spectra

Tables II-IV list the neutron yields as a function of energy from carbon, oxygen, and calcium at various $n\text{-}\gamma$ angles. The bin width represents approximately the FWHM energy resolution of the system. Backgrounds have been subtracted. The spectra were corrected for the energy dependent neutron detector efficiency. In addition, neutrons were lost because the separation of neutron and photon signals in the $n\text{-}\gamma$ discrimination was not complete and was pulse height dependent. Appropriate compensation for these losses and for attenuation of neutrons by the target and shielding were made. The energy spectrum for each element, integrated over all angles, is displayed in Fig. 7.

The structure below 5 MeV in the carbon and oxygen spectra was not due to the neutron counter threshold as no such structure was seen in neutron energy spectra from all stopping pions.

The total neutron yield per radiative pion capture in the energy interval 1.7 to 28.3 MeV was 0.76 ± 0.01 for carbon, 0.70 ± 0.01 oxygen, and 0.81 ± 0.02 for calcium, where the errors are purely statistical. No attempt was made to account for the contributions from the target containers.

3. Angular correlations

Figure 8 shows the angular distributions binned by neutron energies for carbon, oxygen, and calcium. These distributions are not isotropic. The data show peaks at 180° for the higher energy interval becoming more symmetric about 90° for the lower intervals. Over the entire energy interval, 1.7 to 28.3 MeV, this maximum isotropic component is 67% of the total yield for carbon, 74% for oxygen, and 71% for calcium.

IV. EXPERIMENTAL RESULT

First we discuss the structure in the neutron spectra and the energy dependence of the $n\text{-}\gamma$ angular correlations in a direct emission model. Second we investigate the same for a resonance process. We treat these two processes as incoherent, which may be correct in practice.

A. Direct neutron emission

We calculated the radiative pion capture rates as a function of the emergent neutron energy and the $n\text{-}\gamma$ angular correlation, using distorted wave techniques.¹³ The initial state proton wave function was described with an independent particle model and a Wood-Saxon potential using the parameters of Elton and Swift.¹⁴

Final state interactions between the neutron and the residual nucleus were calculated in an optical model the parameters of which are known only qualitatively. We studied various choices of parameters and the results for ^{12}C appear in Table V. Since the Born calculation is equivalent to a closure approximation of the capture rates, the effect of the distortion appears in the fraction of

direct emission neutrons. The number of direct neutrons depends strongly on the presence of final state interactions, but is insensitive to reasonable variations in the absorption parameter as are the energy spectrum and the angular correlations.

To obtain absolute yields, we normalized the calculated direct emission energy spectrum to the experimental data above about 10 MeV. Neutron yields from the direct emission estimate are compared with the experimental yields in Table VI. The contribution of this direct emission process is indicated by the solid curves in Fig. 7 for neutron energy spectra and Fig. 8 for $n\text{-}\gamma$ angular

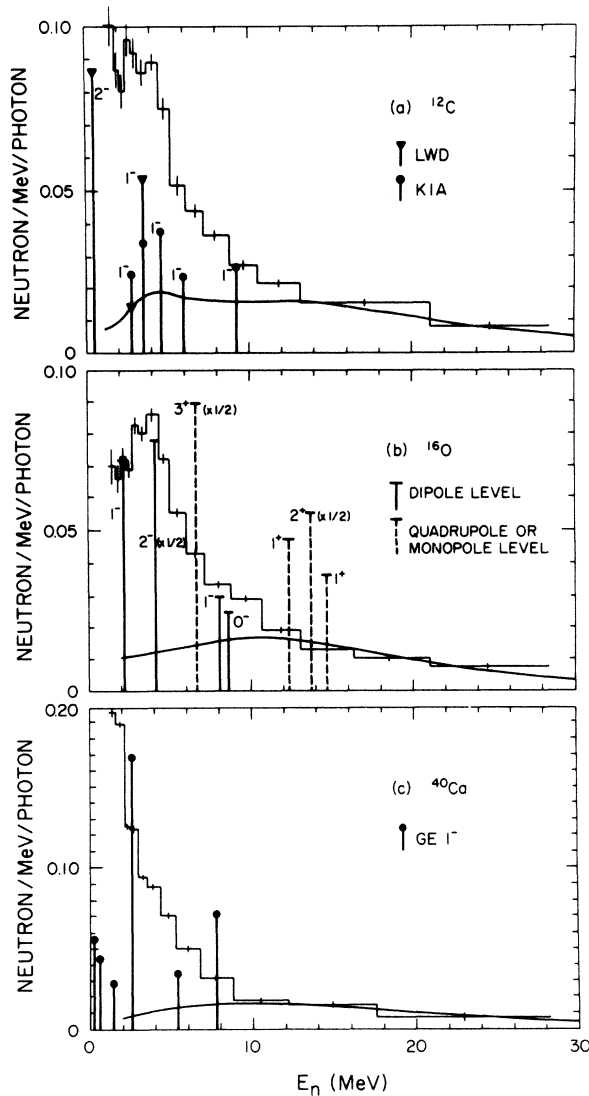


FIG. 7. Neutron energy distributions integrated over all angles for (a) carbon, (b) oxygen, and (c) calcium. The solid curves are the normalized theoretical neutron yields due to the direct emission mechanism. The method of normalization is described in Sec. IV A.

TABLE V. Model parameters and number of direct neutrons emitted following radiative pion capture by ^{12}C .

Model	Neutron potential parameters (MeV)	Relative number of neutrons
Born	None	1.00
Wood-Saxon	$\text{Re}(V) = 50, \text{Im}(V) = 0$	0.54
	$\text{Re}(V) = 50, \text{Im}(V) = 5$	0.30
	$\text{Re}(V) = 50, \text{Im}(V) = 7.5$	0.25
Bjorklund-Fernbach ^a	Energy dependent	0.21

^a Reference 15.

correlations.

For the highest energy bins in Fig. 8, the calculation reproduces the $n\text{-}\gamma$ correlation at $\theta_{n\gamma} > 90^\circ$ for all targets. There is, however, an excess of events at small angles, and an indication of a maximum at $\theta_{n\gamma} = 0$. These effects persist in the lower energy bins. Thus, either our normalization of the theoretical direct emission spectrum is incorrect or the direct and resonant emissions interfere strongly, modifying the distributions.¹⁶

The calculated direct emission angular correlation in the lower energy bins makes a small contribution to the total neutron yield. Its angular dependence is such that, when subtracted, the resulting nondirect component has an angular dependence nearly symmetric about, and with a minimum near, 90° . This situation is in contrast with photon-neutron angular distributions in the region of the giant dipole resonance, which have maxima at 90° .¹⁷

B. Resonant neutron emission

1. Neutron energy spectra

Inelastic electron scattering provides information on the energy and spin-parity assignments of $T = 1$ levels of our target nuclei.¹⁸⁻²⁷ The energy of the analog states in ^{12}B , ^{16}N , and ^{40}K can be deduced assuming isospin symmetry and correcting for the Coulomb energy difference.

Tables VII-IX list excitation energies $\omega_a(T_3)$ from (e, e') experiments and neutron kinetic energies calculated for these excitations. The theoret-

TABLE VI. Neutron yields.

Target	Neutrons/radiative capture Experimental	Estimated direct yield Number	%
^{12}C	0.756 ± 0.008	0.42 ± 0.01	55
^{16}O	0.694 ± 0.006	0.36 ± 0.01	52
^{40}Ca	0.810 ± 0.024	0.36 ± 0.02	44.5

cal excitation energies $\omega_i(-1)$ correspond to $\omega_e(-1)$, and $Y_n(J^\pi)$ are the theoretical neutron yields per photon.^{8, 9, 28} Pionic atom data is summarized in Ref. 3.

The uncertainty of the theoretical neutron line widths and the unknown contribution of low energy evaporation neutrons prevent us from reconstructing spectra from the theoretical models.

a. ¹²C. Kelly and Überal⁸ calculated strengths of excitations leading to the giant resonances with the Kamimura-Ikeda-Arima model (KIA)²⁹ and the Lewis-de Forest-Walecka model (LWD).³⁰ Only strongly excited states which give neutrons in our

energy range and are associated with observed (e, e') levels are listed in Table V. Neutron yields per photon from these levels shown in Fig. 7(a) were calculated assuming a square distribution 1 MeV wide.

The positive parity and 4^- states have not been calculated. Only one 2^- state has been calculated and its neutrons were of too small energy to be detected. The dominant contribution to the observed structure is from the group of 1^- levels which comprise the giant resonance. The spread of the excitation strength is best represented by the KIA model. The LWD model has $\omega_i(-1) \sim 1.5$

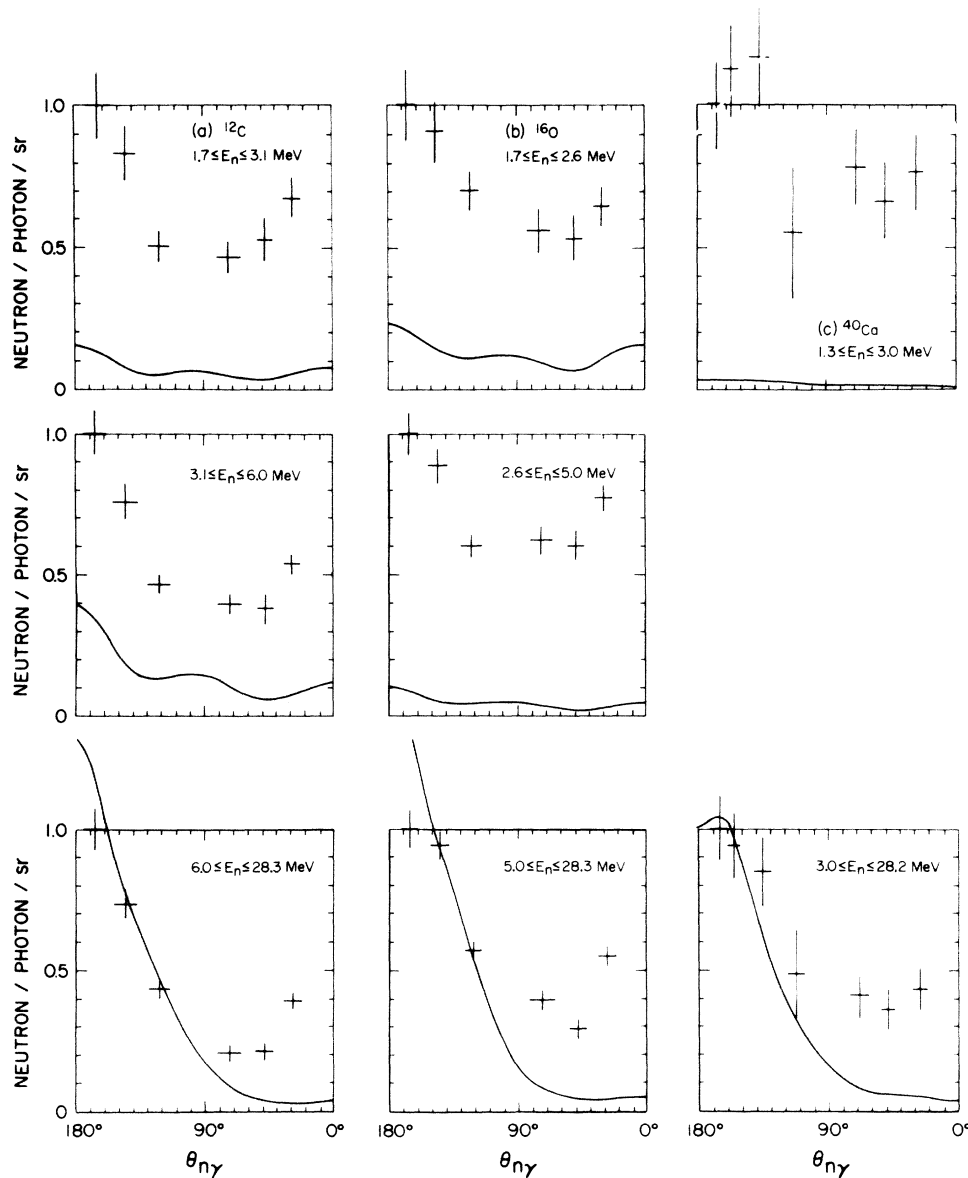


FIG. 8. Angular distributions for (a) carbon, (b) oxygen, and (c) calcium. The solid curves are the normalized theoretical n - γ angular correlations. The normalization used is identical to that of Fig. 7.

TABLE VII. Predicted excitation energies, neutron energies, and yields for ^{12}C radiative pion capture.

Level J^π	(e, e') experiments ^a			LWD ^b		KIA ^b	
	$\omega_e(0)$ (MeV)	$\omega_e(-1)$ (MeV)	E_n^c (MeV)	$\omega_t(-1)$ (MeV)	$Y_n(J^\pi)^d$ (per photon)	$\omega_t(-1)$ (MeV)	$Y_n(J^\pi)^d$ (per photon)
2^-	19.3 ^{e-g}	17.6	0.2	19.1	0.086	16.9	...
4^-	19.6 ^{e-g}	17.9	0.3
2^+	20.0 ^e	18.3	0.9
3^+	20.6 ^e	18.9	1.4
3^-	21.6 ^e	19.9	2.3
1^-	22.0 ^e	20.3	2.7	21.6	0.015	19.5	0.025
2^-	22.2	0.034	20.3	0.046
1^-	22.7 ^e	21.0	3.4	23.3	0.054	21.3	0.034
1^-	23.8 ^e	22.1	4.4	22.3	0.038
1^-	25.5 ^e	23.8	5.9	23.7	0.023
1^-	29.0 ^e	27.3	9.1	25.6	0.014
						26.7	0.008
						27.7	0.007

^a Measured from the ground state of the $T_3 = 0$ nucleus.

^b Reference 8.

^c Calculated from $\omega_e(-1)$, after corrections for nuclear recoil and electron loss.

^d For an excited state J^π .

^e Reference 21.

^f Reference 19.

^g Reference 20.

MeV too high, which is consistent with the observed photon spectrum of this reaction³ and the neutron spectrum from muon capture.³¹

b. ^{16}O . Murphy *et al.*, using the generalized

Goldhaber-Teller model, calculated the excitation strengths for this reaction.⁹ They included the dipole³² and quadrupole³³ resonance levels. We used these strengths and the neutron branching ratio to

TABLE VIII. Predicted excitation energies, neutron energies, and yields for ^{16}O radiative pion capture.

Level J^π	(e, e') experiments ^a				Murphy <i>et al.</i> , ^b			Hill-Überall ^c
	$\omega_e(0)$ (MeV)	$\omega_e(-1)$ (MeV)	E_n^d (MeV)		$\omega_t(-1)$ (MeV)	$Y_n(J^\pi)^e$ (per photon)		$\omega_t(0)$ (MeV)
			n_1	n_2		n_1	n_2	
2^-	17.60 ^f	15.6	1.6	18.7
2^-	19.04 ^f	16.5	2.9	20.0
1^-	20.95 ^f	18.4	4.7	21.0
	19.5 ^f	17.0	3.3
	19.0 ^f	16.5	2.9
2^-	20.4 ^f	17.9	4.2	...	17.5	0.148	...	21.3
3^+					20.5	0.179
2^-	23.3 ^g	20.8	7.0	0.3	24.5
1^-	24.4 ^g	21.9	8.0	2.0	22.0	0.072	0.030	26.6
0^-	22.5	0.025	...	29.0
2^+	28.1	0.110
1^+	29.1	0.179	...	29.0

^a Measured from the ground state of the $T_3 = 0$ nucleus.

^b Reference 9.

^c Reference 28.

^d Calculated from $\omega_e(-1)$ after correction for nuclear recoil and electron loss. n_1 (n_2) are neutrons leading to the ground (one hole excited) state of the final nucleus.

^e For an excited state J^π .

^f Reference 23.

^g Reference 24.

TABLE IX. Predicted excitation energies, neutron energies, and yields for ^{40}Ca radiative pion captures.

Level J^π	$(e, e'), (p, \gamma), (\gamma, n)$ experiments ^a					Hill-Überall ^b	Guy-Eisenberg ^c			
	$\omega_e(0)$	$\omega_e(-1)$	E_n^d			$\omega_f(-1)$	$\omega_f(-1)$	$Y_n(J^\pi)^e$		
	(MeV)	(MeV)	n_1	n_2	n_3	(MeV)	(MeV)	n_0	n_1	n_2
1^-	24.0 ^f	17.7	7.9	5.4	1.7	17.2	14.9	0.072	0.035	0.030
2^-	21.3 ^{f-h}	15.0	5.2	2.8	...	15.8
2^-	19.2 ^{f-h}	12.8	3.1	1.2	...	13.1
1^-	18.7 ^{f-i}	12.3	2.6	0.6	...	11.8	12.8	0.17	0.044	...
2^-	17.6 ^{g,h}	11.2	1.5	11.1
1^-	16.2 ^{f-h,j}	9.8	0.2	9.7	8.7	0.057
2^-	15.5 ^{f-h,j}	9.1	10.0

^a Measured from the $T_3 = 0$ nucleus ground state.

^b Reference 38.

^c Reference 34.

^d Calculated from $\omega_e(-1)$ after corrections for nuclear recoil and electron loss. $n_0, n_1,$ and n_2 are neutrons from the ground state and to the first two one-hole excited states.

^e For an excited state J^π .

^f Reference 27.

^g Reference 25.

^h Reference 26.

ⁱ Reference 38.

^j Reference 37.

the first one-neutron hole excited state of ^{15}N to calculate the neutron yields, which are displayed in Fig. 7(b).

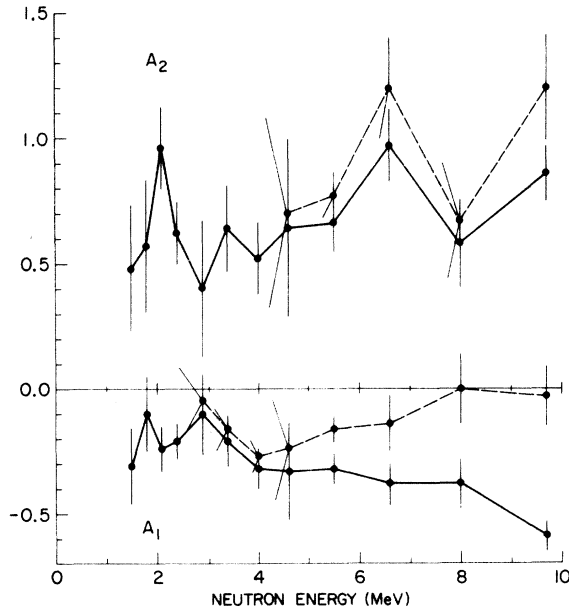


FIG. 9. Legendre polynomial coefficients A_1 and A_2 as a function of the neutron energy for carbon. The solid lines connect the values of A_1 and A_2 obtained without subtraction of the normalized direct emission neutrons. The dotted lines are for the values of A_1 and A_2 obtained after the subtraction.

Prominent are neutrons from the $2^-(E_n = 4.2 \text{ MeV})$ and the $1^-(E_n = 8.0 \text{ and } 2.0 \text{ MeV})$ levels which are spin-isospin states. The 2^- level has been also seen in the photon spectrum,³ and in the neutron spectrum obtained by Holland, Minehart, and Sobottka.¹⁰ The contribution from the quadrupole states, if any, is much smaller than predicted.

c. ^{40}Ca . Guy and Eisenberg have shown that for medium mass nuclei, the distribution of the spin-isospin strength among levels of a given J^π is much more fragmented than in light nuclei.³⁴ Besides, the neutrons leading to the ^{39}K single hole excited states ($\frac{5}{2}^+$ at 15.46 MeV and $\frac{1}{2}^+$ at 11.64 MeV) also wash out structure in the spectrum. Thus, it is not surprising that the neutron energy spectrum is devoid of resonance structure. Excitation strengths of the 1^- states in ^{40}K due to $2p$ pion absorption³⁴ were used to calculate the neutron distribution given in Fig. 7(c). The neutron energies were calculated from the observed (e, e') , (p, γ) , and (γ, n) levels, and the positions of the ^{39}K single hole states.³⁵

2. Angular correlation

As we previously pointed out, the $n-\gamma$ angular correlation can be used to verify the spin and parity assignment of a giant resonance state by expanding in terms of a Legendre polynomial $1 + A_1 P_1 + A_2 P_2 + \dots$. For ^{12}C the dominant contribution is from electric dipole, with a computed A_2 of 0.43 ± 0.24 . The experimental data were fitted to the

second order of the Legendre polynomial; results are shown in Fig. 9. The value of $A_2=0.6$ averaged over the energy range of 1–5 MeV is in qualitative agreement with a $J^\pi = 1^-$ axial vector level. The subtraction of the direct emission neutrons produced vanishing A_1 at higher energies as expected, but did not substantially alter A_2 .

We performed the same fitting procedure to the oxygen data. However, the χ^2 obtained for the fourth order Legendre fit necessitated by both 1^- and 2^- states being present was too large to justify any conclusion.

For ^{40}Ca the absence of resonance structure in the spectrum and the insufficient knowledge of the contribution from quadrupole and positive parity states make the procedure suspect.

ACKNOWLEDGMENTS

The authors are grateful to the Space Radiations Effects Laboratory for their excellent support during this experiment. Professor D. K. Anderson provided the calculation of the direct emission model and many useful discussions.

*This work was supported in part by a grant from the National Aeronautic and Space Administration.

†Submitted in partial fulfillment of the requirements for the Ph.D. degree at Virginia Polytechnic Institute and State University.

‡Present address: Lawrence Berkeley Laboratory, Berkeley, California 94720.

¹V. I. Petrukhin and Yu. D. Prokoshkin, *Nucl. Phys.* **66**, 669 (1965).

²H. Davies, M. Muirhead, and J. N. Wouds, *Nucl. Phys.* **78**, 673 (1966).

³J. A. Bisterlich, K. M. Crowe, A. S. L. Parsons, P. Skarek, and P. Trüöl, *Phys. Rev. C* **5**, 1867 (1972).

⁴J. Delorme and T. E. O. Ericson, *Phys. Lett.* **21**, 98 (1966).

⁵D. K. Anderson and J. M. Eisenberg, *Phys. Lett.* **22**, 164 (1966).

⁶L. G. Dakhno and Yu. D. Prokoshkin, *Yad. Fiz.* **7**, 565 (1968) [transl.: *Sov. J. Nucl. Phys.* **7**, 351 (1968)].

⁷L. C. Foldy and J. D. Walecka, *Nuovo Cimento* **34**, 1026 (1964).

⁸F. J. Kelly and H. Überall, *Nucl. Phys.* **A118**, 310 (1968).

⁹J. D. Murphy, R. Raphael, H. Überall, R. E. Wagner, D. K. Anderson, and C. Werntz, *Phys. Rev. Lett.* **19**, 714 (1967).

¹⁰J. C. Alder, C. Joseph, B. Vaucher, T. Bressani, E. Chivassa, D. Shinzel, J. Favies, and C. Zupancic, *Nuovo Cimento Lett.* **4**, 256 (1970); M. M. Holland, R. C. Minehart, and S. E. Sobottka, *Nucl. Phys.* **A147**, 249 (1970).

¹¹F. D. Brook, *Nucl. Instrum. Methods* **4**, 151 (1959).

¹²R. E. Textor and V. V. Verbinski, Oak Ridge National Laboratory Report No. ORNL-4160, UC-34-Physics.

¹³D. K. Anderson, to be published.

¹⁴L. R. B. Elton and A. Swift, *Nucl. Phys.* **A94**, 52 (1967).

¹⁵F. Bjorklund and S. Fernbach, *Phys. Rev.* **109**, 1295 (1958).

¹⁶W.-C. Lam, K. Gotow, B. Macdonald, W. P. Trower, and D. K. Anderson, *Phys. Rev. Lett.* **28**, 108 (1972).

¹⁷E. Hayward, in *Nuclear Structure and Electromagnetic Interactions*, edited by N. Macdonald (Plenum, New York, 1965), p. 141.

¹⁸T. De Forest, Jr., J. D. Walecka, G. Vanpraet, and

W. C. Barber, *Phys. Lett.* **16**, 311 (1965).

¹⁹L. W. Donnelly, J. D. Walecka, I. Sick, and E. B. Hughes, *Phys. Rev. Lett.* **21**, 1196 (1968).

²⁰P. Antony-Spies, P. P. Delsanto, E. Spamer, A. Goldmann, and O. Titze, *Phys. Lett.* **31B**, 632 (1970).

²¹Y. Torizuka, A. Yamaguchi, T. Terasawa, Y. Kajima, K. Nakahara, M. Oyamada, K. Itoh, A. Nakada, S. Mitunobu, and M. Kimura, *Phys. Rev. Lett.* **25**, 874 (1970).

²²M. Stroetzel, *Z. Phys.* **214**, 357 (1968).

²³M. Stroetzel and A. Goldmann, *Z. Phys.* **233**, 245 (1970).

²⁴A. Goldmann and M. Stroetzel, *Z. Phys.* **239**, 235 (1970).

²⁵A. Goldmann, *Z. Phys.* **234**, 144 (1970).

²⁶K. Itoh, M. Oyanada, and Y. Torizuka, *Phys. Rev. C* **2**, 2181 (1970).

²⁷J. P. Perez, Y. Jorba, and H. Nguyen Ngoc, *J. Phys. Radium* **22**, 551 (1961).

²⁸L. H. Hill and H. Überall, *Nucl. Phys.* **A190**, 341 (1972).

²⁹M. Kamimura, K. Ikeda, and A. Arima, *Nucl. Phys.* **A95**, 129 (1967).

³⁰F. H. Lewis and J. D. Walecka, *Phys. Rev.* **133**, B849 (1964); T. deForest, Jr., *ibid.* **139**, B1217 (1965); V. Gillet and N. Vinh Mau, *Nucl. Phys.* **54**, 321 (1964); G. E. Brown, L. Costillejo, and J. A. Evans, *ibid.* **22**, 1 (1961).

³¹E. Plett and E. Sobottka, *Phys. Rev. C* **3**, 1003 (1971).

³²R. Raphael, H. Überall, and C. Werntz, *Phys. Lett.* **24B**, 15 (1967).

³³B. M. Spicer and J. M. Eisenberg, *Nucl. Phys.* **63**, 520 (1965).

³⁴R. Guy and J. M. Eisenberg, *Phys. Lett.* **33B**, 137 (1970).

³⁵P. M. Endt and C. Van Der Leun, *Nucl. Phys.* **A105**, 1 (1967). Also see Ref. 36.

³⁶L. J. Weigrt and J. M. Eisenberg, *Nucl. Phys.* **53**, 508 (1964).

³⁷B. I. Goryachev, B. S. Ishkanav, B. G. Shevchenko, and B. A. Yur'ev, *Yad. Fiz.* **5**, 1138 (1969) [transl.: *Sov. J. Nucl. Phys.* **5**, 811 (1967)].

³⁸F. W. K. Firk, *Nucl. Phys.* **52**, 437 (1969).